PCCP

ROYAL SOCIETY OF CHEMISTRY

PAPER

View Article Online
View Journal

Cite this: DOI: 10.1039/d6cp00979d

Is range separation always necessary for modeling TADF emitters? A benchmark study of B3LYP on dispersion-corrected geometries *vs.* tuned ωB97X-D

Sanyam, † Nishi Tejiyan,† Krishna Singh and Anirban Mondal *

Thermally activated delayed fluorescence (TADF) emitters are commonly modeled using optimally tuned range-separated density functionals to capture their charge-transfer–dominated excited states. However, the necessity of such tuning remains an open question, particularly in view of its substantial computational cost. In this work, we present a systematic benchmark of density functional methods for predicting the ground- and excited-state properties of TADF molecules, based on a dataset of 26 experimentally reported emitters spanning diverse donor–acceptor architectures. We compare the performance of B3LYP augmented with Grimme's D3 dispersion correction (B3LYP-D3) against optimally tuned ω B97X-D, M06-2X, and related variants. The assessment covers frontier orbital energies, singlet and triplet excitation energies, singlet–triplet gaps, radiative and non-radiative rate constants, and exciton charge-transfer descriptors. Within the computational protocol employed here, we find that B3LYP-D3 provides consistent predictions for several ground-state properties and yields singlet–triplet energy gaps and photophysical rate constants that are comparable to those obtained with optimally tuned functionals. While tuning the range-separation parameter can improve the description of certain excited-state energies, these gains are not systematic across the dataset and must be considered alongside the associated computational overhead. Taken together, the results indicate that, within the present workflow, fortuitous error cancellation enables dispersion-corrected B3LYP geometries to achieve performance comparable to that of more computationally demanding, tuned range-separated functionals for this specific class of molecules. This observation suggests that B3LYP-D3 may offer a computationally efficient option for exploratory calculations and preliminary screening of TADF emitters, though care must be taken as these findings may not be directly transferable to other architectural or architectural-system classes not investigated here.

Received 17th March 2026,
Accepted 6th June 2026

DOI: 10.1039/d6cp00979d

rsc.li/pccp

1 Introduction

Thermally activated delayed fluorescence (TADF) has emerged as a cornerstone strategy for realizing highly efficient organic light-emitting diodes (OLEDs). By enabling the upconversion of non-emissive triplet excitons to emissive singlet states through reverse intersystem crossing (RISC), TADF emitters allow for the theoretical utilization of both singlet and triplet excitons, achieving up to 100% internal quantum efficiency (IQE).[1–3] Depending on their electronic architecture, TADF materials are generally categorized into two major classes: donor–acceptor–donor (D–A–D) type and multi-resonant (MR-TADF) emitters.

In D–A–D systems, donor and acceptor moieties are linked through single bonds or flexible spacers, promoting spatial separation between the highest occupied molecular orbital (HOMO) and the lowest unoccupied molecular orbital (LUMO).[2,4–6] This orbital separation effectively reduces the exchange interaction and thus narrows the singlet–triplet energy gap (ΔE_{ST}), which is essential for efficient RISC. Conversely, MR-TADF emitters feature rigid polycyclic frameworks incorporating heteroatoms such as boron (B), nitrogen (N), sulfur (S), and oxygen (O).[7–9] Their unique resonance-induced frontier orbital distribution simultaneously ensures a small ΔE_{ST} and high oscillator strength, enabling narrowband emission.

The performance of TADF emitters is governed by a delicate interplay of several key parameters—the singlet–triplet energy gap (ΔE_{ST}), spin–orbit coupling $\left(H_{SO}^{S_1T_1}\right)$, reorganization energy (λ), and both radiative (k_R) and non-radiative (k_{NR}) decay rate

Department of Chemistry, Indian Institute of Technology Gandhinagar, Gujarat, 382355, India. E-mail: amondal@iitgn.ac.in
† Contributed equally to this work.

constants. Achieving fast RISC requires a sufficiently small ΔE_{ST} and sizable $H_{SO}^{S_1T_1}$ between the lowest singlet (S_1) and triplet (T_1) excited states. Therefore, accurate computation of these parameters is crucial for understanding exciton dynamics and for rational molecular design of efficient emitters.[10–18]

Computational modeling, particularly density functional theory (DFT) and time-dependent DFT (TD-DFT), has become indispensable for predicting and rationalizing the optoelectronic behavior of TADF molecules.[19–22] However, the predictive reliability of these methods is highly sensitive to the choice of exchange–correlation functional. While TD-DFT accurately describes charge-transfer (CT) excitations in most D–A–D TADF emitters, it struggles to capture the excited-state features of MR-TADF systems, primarily due to its inability to properly account for double excitations that dominate in these rigid frameworks.[20,22] In this context, double-hybrid functionals such as B2PLYP have been shown to perform well for MR-TADF systems owing to their improved description of double excitations in the singlet state.[20,23] However, for D–A–D systems, where single excitations predominate, TD-DFT remains both robust and computationally efficient.[24–26] Consequently, the routine use of double-hybrid functionals for D–A–D emitters is often impractical due to their substantially higher computational cost. To improve accuracy, the community has largely adopted optimally tuned range-separated hybrid functionals, particularly ωB97XD, which balance local and long-range exchange interactions.[27] These functionals deliver superior predictions for both local and CT excitations but at a significant computational expense, as the range-separation parameter must be optimized for each molecule. This optimization step poses a severe bottleneck for high-throughput screening and design of new emitters. Consequently, there is growing interest in identifying cost-effective yet reliable alternatives—such as hybrid functionals with dispersion corrections (*e.g.*, B3LYP-D3) and long-range corrected functionals like M062X—to achieve a favorable balance between accuracy and computational efficiency.[24,25]

In this work, we contest the prevailing notion that optimally tuned range-separated functionals are indispensable for reliable prediction of TADF properties. We hypothesize that the widely used B3LYP functional, when combined with Grimme's D3 dispersion correction (B3LYP-D3), can offer predictive accuracy comparable to that of ωB97XD across diverse classes of TADF molecules. To test this hypothesis, we carry out a systematic benchmarking study involving 26 experimentally reported TADF emitters.[2,28–43] The performance of B3LYP-D3 is compared against DFT functionals including ωB97XD, M06-2X, and B3LYP-D3(BJ) (which includes short-range dispersion corrections) through comprehensive evaluation of both ground- and excited-state properties. Specifically, we examine HOMO–LUMO energy levels, singlet (S_1) and triplet (T_1) energies, and excitonic descriptors such as the charge-separation distance (D_{CT}) and charge-transfer number (Q_{CT}). Furthermore, key kinetic parameters–including prompt fluorescence (k_{PF}), intersystem crossing (k_{ISC}), and reverse intersystem crossing (k_{RISC}) rates–are computed to assess how well each functional captures excited-state dynamics. While optimally tuned range-separated functionals do yield improved accuracy for certain excited-state properties in specific cases, these improvements are neither systematic nor substantial across the full dataset and come at a significantly higher computational cost due to the need for molecule-specific parameter tuning. Through this systematic comparison, we demonstrate that B3LYP-D3 provides a computationally efficient yet quantitatively reliable route for modeling TADF materials, offering a practical alternative for large-scale screening and rational design of next-generation OLED emitters.

The motivation for this work was not based on the hypothesis that a conventional hybrid functional is inherently superior to optimally tuned range-separated hybrids (OT-RSHs). Rather, it arose from two considerations. First, previous studies—including ref. 44—have shown that global hybrids can sometimes reproduce singlet–triplet gaps with reasonable accuracy due to error compensation between singlet and triplet excitation energies. In addition, conventional hybrids such as B3LYP remain widely used for practical computational screening of TADF emitters due to their robustness and lower computational cost. As discussed in a recent study,[45] deviations in certain RSHs can arise from significant short-range HF exchange contributions or non-optimal range-separation parameters. At the same time, analyses reported in ref. 46 demonstrate that carefully constructed OT-RSHs—particularly those without short-range HF exchange and with correct asymptotic behavior—can provide systematically improved excited-state descriptions for TADF systems in both gas and solvent phases when benchmarked against experimental and high-level theoretical data. Regarding the choice of B3LYP-D3, it was selected because (i) it remains one of the most commonly employed functionals in the TADF literature, (ii) its performance in predicting ΔE_{ST} and excitation energies is well documented, and (iii) the inclusion of dispersion corrections enables a more balanced description of ground-state structures and noncovalent interactions relevant to these emitters. The objective of the present study is therefore to benchmark a widely used and computationally efficient protocol against OT-RSH approaches within the same computational framework, rather than to establish a general hierarchy of DFT approximations.

2 Computational methodology

We employed a comprehensive computational protocol to investigate a curated set of 26 experimentally reported donor–acceptor–donor type TADF emitters obtained from the literature.[2,28–43] The chemical structures of these molecules are illustrated in Fig. 1. As shown, the selected compounds encompass a broad chemical space through systematic variations in donor–acceptor combinations, π-conjugation lengths, and electron-donating or -withdrawing substituents. All molecules adhere to a donor–acceptor (D–A) molecular design, where the spatial separation of frontier orbitals governs the photophysical properties. Representative examples such as 2,3-TXO-PhCz, 2,5-Cz, and TXO-PhCz exhibit a direct D–A linkage, while others

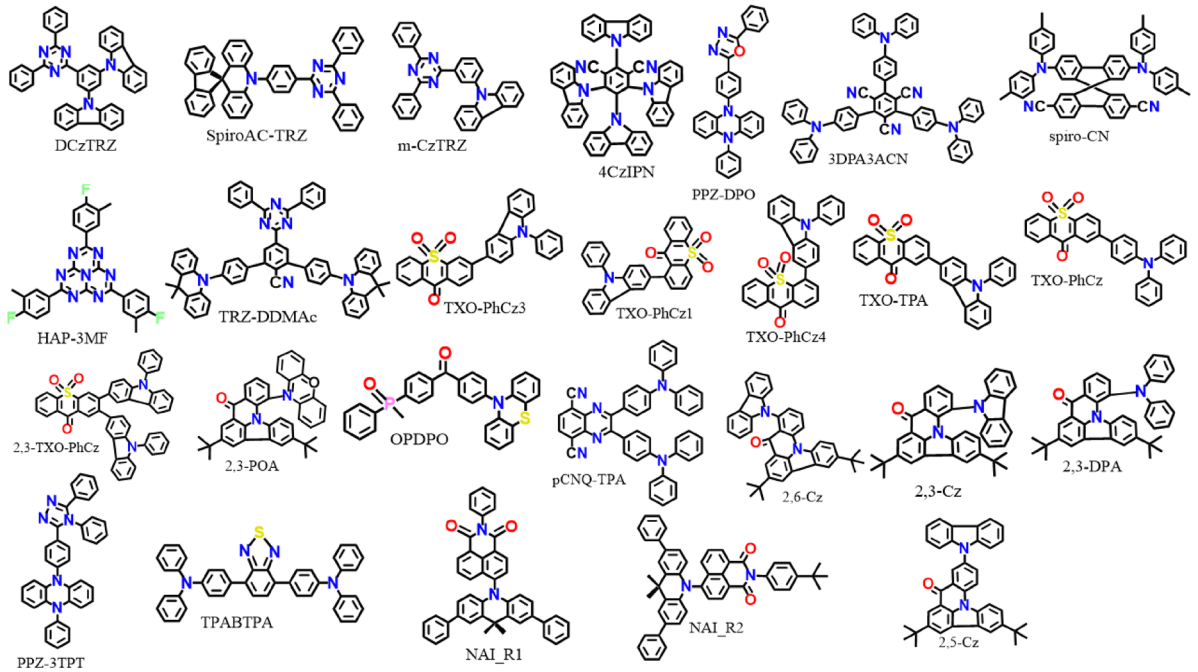

Fig. 1 Chemical structures of the investigated compounds in the present study.[2,28–43]

incorporate phenyl bridges between donor and acceptor fragments to fine-tune conjugation and electronic coupling. The acceptor components commonly include strong electron-withdrawing units such as cyano groups, triazine moieties (aromatic rings containing three nitrogen atoms), and fluorine substituents. Additional electron-deficient functionalities, such as carbonyl and sulfoxide groups, are also present in several compounds. On the donor side, carbazole units are frequently employed—for instance, in DCzTRZ and TXO-TPA—and are known for their moderate electron-donating ability and structural rigidity. *N*,*N*-diphenylamine derivatives are also widely used as donor fragments, offering enhanced conjugation and tunable electronic interactions. In a few cases, sulfur- and phosphorus-containing groups are incorporated to promote spin–orbit coupling, thereby facilitating efficient intersystem crossing. Overall, the chosen set of molecules represents prototypical D–A systems characterized by spatially separated HOMOs and LUMOs. This separation leads to small singlet–triplet energy gaps, which favor efficient reverse intersystem crossing. The chemical and electronic diversity within this dataset thus makes it ideally suited for benchmarking the accuracy and transferability of different density functional approximations in modeling TADF-active materials.

All quantum-chemical calculations were carried out in the gas phase using the Gaussian09 software package,[47] and molecular visualizations were generated using GaussView. Ground-state geometries of all 26 TADF emitters were optimized without symmetry constraints to ensure accurate electronic structure characterization. To achieve a balance between computational efficiency and predictive accuracy, we employed five exchange–correlation functionals—ωB97XD, tuned-ωB97XD (ω'B97XD), B3LYP-D3, B3LYP-D3(BJ), and M06-2X—in conjunction with the 6-31+G(d,p) basis set.[48–51] To ensure high numerical precision and reproducibility, the self-consistent field (SCF) energy convergence threshold was strictly set to 1.0×10^{-8} a.u. on the density matrix. Geometry optimizations were performed in redundant internal coordinates using standard convergence thresholds: maximum force $<4.5 \times 10^{-4}$ a.u., root-mean-square (RMS) force $<3.0 \times 10^{-4}$ a.u., maximum displacement $<1.8 \times 10^{-3}$ a.u., and RMS displacement $<1.2 \times 10^{-3}$ a.u. All numerical integrations for the underlying DFT exchange–correlation kernels and their TD-DFT extensions were executed using a pruned fine integration grid to guarantee numerical stability, energy conservation, and rotational invariance.

The optimally tuned range-separated functional (ω'B97XD) was parameterized following the procedure described in ref. 27,52–56. In this approach, the range-separation parameter (ω) is adjusted to minimize the deviation between the ionization potential (IP) and the negative of the highest occupied molecular orbital (HOMO) energy, thereby ensuring consistency with Koopmans' theorem. The optimized ω value was obtained by minimizing the objective function

$$J(\omega) = (E_{\mathrm{HOMO}}^{\mathrm{neutral}} + \mathrm{IP})^2 + (E_{\mathrm{LUMO}}^{\mathrm{neutral}} + \mathrm{EA})^2, \quad (1)$$

where $E_{\mathrm{HOMO}}^{\mathrm{neutral}}$ and $E_{\mathrm{LUMO}}^{\mathrm{neutral}}$ correspond to the highest occupied and lowest unoccupied molecular orbital energies of the neutral species, respectively. The ionization potential and electron affinity (EA) were obtained from total energy differences as follows:

$$\mathrm{IP} = E_{\mathrm{cation}} - E_{\mathrm{neutral}}, \quad (2)$$

$$\mathrm{EA} = E_{\mathrm{neutral}} - E_{\mathrm{anion}}, \quad (3)$$

where E_{cation}, E_{neutral}, and E_{anion} denote the total electronic energies of the cationic, neutral, and anionic species, respectively. This tuning ensures consistency between orbital energies

and the corresponding charged species, thereby improving the accuracy of excitation energy predictions.

Following the optimal tuning of the range-separation parameter, excited-state single-point calculations were carried out for all molecules to determine the first singlet (S_1) and triplet (T_1) excitation energies. The singlet–triplet (ST) energy gap was subsequently computed as the energy difference between these states. The ST gaps were computed as vertical gaps, *i.e.*, singlet and triplet excitation energies were evaluated at the optimized ground-state geometry. This choice was made to ensure methodological consistency across the entire molecular set and to allow a direct comparison of single-point excited-state energies among the different functionals. Since the primary objective of this study is a comparative assessment of functional performance across multiple photophysical descriptors, a uniform vertical protocol was adopted to avoid introducing additional variability arising from functional-dependent excited-state structural relaxation. For emission energies, however, the excited-state geometries were explicitly optimized (within the respective method), and vertical emission energies were computed from those optimized structures. Thus, relaxation effects were included in the fluorescence energies. Although the adiabatic ST gaps and explicit consideration of optimized triplet geometries can provide a more complete physical picture, as demonstrated in earlier TD-DFT/TDA-based investigations.[57] Moreover, such an approach can be particularly important when analyzing the nature of the involved excited states and structural relaxation effects. However, performing full triplet excited-state geometry optimizations for all 26 molecules with all considered functionals would require substantial computational effort and significantly extend the scope of the present benchmarking study. Our intention here was to compare the intrinsic ability of the functionals to reproduce excitation energies and derived properties within a consistent and computationally tractable protocol. To assess the influence of environmental screening, solvent effects were incorporated for a representative subset of five molecules using the conductor-like polarizable continuum model (CPCM) as implemented in Gaussian09, with toluene (ε = 2.38) as the solvent. Solvent stabilization moderately reduced deviations in the computed excitation energies, highlighting its importance in mimicking experimental conditions while maintaining computational tractability.

The accuracy of each functional was quantitatively evaluated by comparing the computed values against available experimental data. For this purpose, statistical performance metrics—mean absolute deviation (MAD), root mean square deviation (RMSD), and standard deviation (σ)—were calculated using the following expressions:

$$\begin{aligned} \mathrm{MAD} &= \frac{1}{N}\sum_{i=1}^{N}\left|x_i - x_i^{\mathrm{ref}}\right|, \\ \mathrm{RMSD} &= \sqrt{\frac{1}{N}\sum_{i=1}^{N}\left(x_i - x_i^{\mathrm{ref}}\right)^2}, \\ \sigma &= \sqrt{\frac{1}{N-1}\sum_{i=1}^{N}\left(x_i - \bar{x}\right)^2}, \end{aligned} \tag{4}$$

where x_i and x_i^{ref} represent the computed and reference (experimental) quantities, respectively, and $\bar{x}$ denotes the mean of the computed dataset. These statistical descriptors provide a robust measure of each functional's predictive reliability across the molecular dataset, enabling a systematic comparison of their accuracy and consistency.

Radiative (k_{PF}) and non-radiative (k_{ISC}, k_{RISC}) rate constants were computed to elucidate the exciton dynamics governing TADF behavior. The radiative rate constant (k_{PF}), corresponding to prompt fluorescence, quantifies the probability of radiative decay from the first excited singlet state (S_1) to the ground state (S_0). It was evaluated using Einstein's spontaneous emission formula:

$$k_{\mathrm{PF}} = \frac{\Delta E_{S_0S_1}^2 f_{S_0S_1}}{1.499}, \tag{5}$$

where $f_{S_0S_1}$ denotes the oscillator strength, and $\Delta E_{S_0S_1}$ represents the transition energy between the ground S_0 and first excited singlet S_1 states, expressed in cm^{-1}. This relationship directly links the transition probability to the optical transition dipole moment, thereby serving as a quantitative descriptor of fluorescence efficiency. The non-radiative pathways were analyzed through the intersystem crossing and reverse intersystem crossing processes, which mediate spin conversion between singlet and triplet manifolds. The k_{ISC} rate characterizes the singlet-to-triplet transition, while k_{RISC} describes the thermally assisted reverse process that regenerates emissive singlet excitons—both being central to the delayed fluorescence mechanism. These rate constants were determined using Fermi's Golden Rule:

$$k_{\mathrm{ISC}}^{\mathrm{IF(R)}} = \frac{2\pi}{\hbar}\left|\langle {}^1\psi_I^0 | H_{\mathrm{SO}} | {}^3\psi_{\mathrm{F}}^0\rangle\right|^2 \mathrm{FCWD}, \tag{6}$$

where H_{SO} represents the spin–orbit coupling (SOC) operator, and FCWD is the Franck–Condon weighted density, which captures the vibrational overlap between the initial and final electronic states. The FCWD term was evaluated as:

$$\mathrm{FCWD} = \frac{1}{\sqrt{4\pi\lambda k_{\mathrm{B}} T}}\exp\left[-\frac{(\Delta E + \lambda)^2}{4\lambda k_{\mathrm{B}} T}\right], \tag{7}$$

where λ denotes the reorganization energy, k_{B} is the Boltzmann constant, T is the absolute temperature (taken as 298 K), and ΔE is the singlet–triplet energy gap. These quantities collectively determine the efficiency of triplet harvesting through RISC, which is central to achieving high internal quantum efficiency in TADF materials.

Although Einstein's formula does not explicitly account for the Herzberg–Teller (HT) effect—*i.e.*, vibronic coupling arising from nuclear motion, which becomes particularly important when the oscillator strength is very small. In the present case, the oscillator strengths are not reasonably very small and fall within the typical range reported for donor–acceptor systems. A rigorous inclusion of the HT effect would require additional rate calculations involving excited-state Hessians and vibronic coupling terms, which are computationally demanding. In the present work, our objective is to compare different rate

expressions within a consistent and simplified theoretical framework. Accordingly, the Einstein formula is employed at the Franck–Condon level to enable a direct methodological comparison. Regarding the ISC/RISC rates, geometry relaxation accompanies the transition between singlet and triplet manifolds. A fully quantitative description would require temperature-dependent spin–orbit coupling within the Fermi's Golden Rule formalism, together with an explicit treatment of vibrational effects. Such a comprehensive treatment has been reported in our previous study on three D–A–D molecules, where we provided a detailed discussion of these aspects.[58] In contrast, the primary aim of the present work is to demonstrate how different theoretical approaches behave when implemented within a simplified Marcus-type framework. While this approximation does not yield quantitatively exact rate constants, it provides valuable physical insight and serves as an efficient and computationally tractable strategy for preliminary material screening.

In addition to rate constants, we analyzed descriptors associated with the excitonic nature of the investigated compounds. The charge-transfer (CT) character was quantified by calculating the CT number and the centroid distance between positive and negative charge barycenters. These parameters provide insight into the spatial distribution and extent of electron–hole separation within the excited state. Transition electron densities were obtained using TD-DFT with the B3LYP-D3 and ω'B97XD functionals in combination with the 6-31+G(d,p) basis set, as implemented in ORCA 5.0. The analysis of CT descriptors was subsequently carried out using the Multiwfn program.[59] The optimized geometries of the 26 molecules in ground and excited states (also in solvent phase) are provided in the supplementary information (SI) folder for clarity and reproducibility.

3 Results and discussion

The rationale for compound selection and the computational protocol have been detailed in the preceding section. All investigated molecules are experimentally reported, and their corresponding photophysical data are provided in the SI. Table S1 provides the mapping between the compound numbers used in this study and their corresponding names in the literature. Since these donor–acceptor molecules exhibit minimal double-excitation character, conventional DFT and TD-DFT methods are sufficient to describe their excited-state properties. Although optimally tuned range-separated hybrid functionals such as ω'B97XD offer improved accuracy, their system-specific nature and high computational cost limit their broader applicability. Therefore, this study aims to establish an efficient and transferable computational strategy that balances accuracy and scalability by benchmarking multiple functionals against available experimental data to capture the essential photophysical descriptors governing TADF behavior. The numerical values of ω as a function of the objective function $J(\omega)$ are provided in Table S13, while the corresponding representative ω *versus* $J(\omega)$ plot is shown in Fig. S15.

3.1 Ground-state properties

It is important to emphasize the nature of the empirical dispersion corrections (D2, D3, and D3(BJ)) employed within our computational workflows. These additive terms are parameterized based on nuclear positions to capture long-range London dispersion effects in the electronic ground state. Because they modify only the total energy and its derivatives (such as gradients and frequencies), they do not alter the underlying electronic structure, molecular orbitals, or electron densities. As a strict mathematical consequence, when calculating vertical excitation or emission energies at a fixed geometry ($E_{\text{vertical}} = E_{\text{state-2}} - E_{\text{state-1}}$), the dispersion energy contributions for both states are identical and cancel out completely. Therefore, the dispersion corrections impact our computed vertical photophysical properties and frontier orbital energies solely through an indirect mechanism: by altering the underlying optimized molecular geometries of the ground or excited states. Any direct differences in electronic transitions or descriptor metrics are governed entirely by the intrinsic performance of the chosen exchange–correlation functional framework.

We begin our analysis with ground-state electronic properties—namely the frontier orbital energies, E_{HOMO} and E_{LUMO}, and their difference, $\Delta E_{\text{HOMO–LUMO}}$. These descriptors were chosen because experimental data are available for most of the compounds, enabling a direct validation of theoretical results. Experimentally reported ''HOMO'' and ''LUMO'' levels are typically derived from oxidation and reduction onset potentials obtained *via* cyclic voltammetry, which are more rigorously related to ionization potentials and electron affinities. This distinction is directly connected to the theoretical foundation of optimal tuning and to the fact that conventional functionals do not strictly satisfy Janak's theorem[60] or the piecewise linearity condition. This approach involved the standard convention in the experimental TADF literature, where oxidation and reduction onsets are frequently reported and interpreted as HOMO and LUMO levels.[29] For consistency with how these values are presented in those studies, the computed Kohn–Sham frontier orbital energies with the reported experimental values were compared. Although such a comparison is not rigorous from a formal electronic-structure standpoint. A more physically meaningful comparison would involve computing vertical IPs and EAs using a ΔSCF protocol and directly relating those quantities to experimental redox potentials. Therefore, comparison of Kohn–Sham eigenvalues with experimental redox-derived quantities should be interpreted qualitatively and trend-wise, rather than as a strict validation of absolute orbital energies. This clarification better delineates the theoretical limitations of the comparison and avoids overinterpretation of the frontier orbital analysis.

Table 1 summarizes the mean absolute deviation, root mean square error, and standard deviation of the calculated properties for the five tested functionals. For E_{HOMO}, both B3LYP-D3 and B3LYP-D3(BJ) deliver the smallest deviations, with MAD and RMSD values of 0.20–0.28 eV and $\sigma \approx 0.20$ eV. In contrast, ωB97XD produces the largest errors (MAD = 1.81 eV, RMSD = 1.83 eV), while its tuned counterpart, tuned-ω'B97XD, shows

Table 1 Mean absolute deviation (MAD), root mean square deviation (RMSD), and standard deviation (σ) of calculated electronic properties across different computational methods. Here, E_{HOMO} and E_{LUMO} denote the highest occupied and lowest unoccupied molecular orbital energies, respectively; is the orbital energy gap; E_{S1} corresponds to the first singlet excited-state energy (absorption or emission); and ΔE_{ST} is the singlet–triplet energy gap. Solvent-corrected values are obtained in toluene with five explicit solvent molecules

Property	B3LYP-D3(BJ)	M06-2X	B3LYP-D3	ωB97XD	ω'B97XD
E_{HOMO}					
MAD	0.20	1.19	0.20	1.81	0.32
RMSD	0.28	1.22	0.28	1.83	0.48
σ	0.19	0.49	0.20	0.29	0.36
E_{LUMO}					
MAD	0.51	1.35	0.50	2.23	1.03
RMSD	0.54	1.38	0.53	2.25	1.10
σ	0.17	0.56	0.18	0.30	0.38
$\Delta E_{HOMO-LUMO}$					
MAD	0.47	2.54	0.47	4.07	0.95
RMSD	0.55	2.56	0.55	4.08	1.18
σ	0.28	0.94	0.29	0.35	0.70
Emission energy (E_{S1})					
MAD	0.55	0.53	0.56	0.68	0.37
RMSD	0.63	0.65	0.64	0.74	0.45
σ	0.31	0.36	0.31	0.29	0.26
Absorption energy (E_{S1})					
MAD	0.41	0.53	0.41	0.72	0.34
RMSD	0.50	0.59	0.50	0.77	0.42
σ	0.71	0.26	0.28	0.27	0.25
ΔE_{ST}					
MAD	0.11	0.27	0.10	0.66	0.11
RMSD	0.13	0.31	0.13	0.67	0.14
σ	0.08	0.26	0.08	0.14	0.08
Solvent-corrected (toluene)					
MAD (E_{S1} emission)	0.41	0.35	0.60	0.61	0.20
RMSD (E_{S1} emission)	0.50	0.38	0.69	0.69	0.24
σ (E_{S1} emission)	0.29	0.16	0.34	0.32	0.14
MAD (E_{S1} absorption)	0.51	0.48	0.53	0.63	0.48
RMSD (E_{S1} absorption)	0.69	0.54	0.71	0.70	0.67
σ (E_{S1} absorption)	0.46	0.26	0.47	0.32	0.46

improved but still inferior performance. The M06-2X functional lies in between, though it exhibits a larger spread (σ = 0.49 eV). A similar trend is observed for E_{LUMO}, where B3LYP-D3 and B3LYP-D3(BJ) again yield the lowest deviations (MAD $\approx$ 0.50 eV, RMSD $\approx$ 0.53 eV), while ωB97XD significantly overestimates the energies (MAD = 2.23 eV, RMSD = 2.25 eV). Tuning the range-separation parameter reduces this error to about 1.0 eV, but the accuracy still falls short of that achieved with the B3LYP-based approaches. For the HOMO–LUMO gap, B3LYP-D3 and B3LYP-D3(BJ) again outperform the other methods, showing excellent agreement with experimental values (MAD = 0.47 eV, RMSD = 0.55 eV). By contrast, the default ωB97XD substantially overestimates the gap (MAD = 4.07 eV, RMSD = 4.08 eV), while tuning reduces the error to 0.95 eV. Fig. S1–S5 visualize the deviation trends. As seen in Fig. S1, the B3LYP-D3 functional (blue bars) consistently yields deviations below 0.83 eV, whereas ω'B97XD (yellow bars) performs reasonably well, except for PPZ-3TPT, which deviates by approximately 1.63 eV. Comparable results are obtained for E_{LUMO} (Fig. S3 and S4), reaffirming the superior accuracy of B3LYP-D3 and B3LYP-D3(BJ) across all metrics.

The HOMO–LUMO gap, being directly linked to the lowest electronic excitation, serves as a critical descriptor for the photophysical behavior of TADF emitters. Fig. 2 compares the deviations in $\Delta E_{HOMO-LUMO}$ obtained from B3LYP-D3 and ω'B97XD. The B3LYP-D3 functional consistently reproduces experimental gaps with minor deviations, confirming its reliability and efficiency for ground-state electronic structure predictions. Absolute values of E_{HOMO}, E_{LUMO}, and $\Delta E_{HOMO-LUMO}$ are provided in Tables S2–S4, with experimental values included where available.

3.2 Excited-state properties

When examining the vertical absorption and emission energies, it is vital to note that the D3 and D3(BJ) empirical corrections do not directly affect these transition metrics. Because vertical transitions are computed at a fixed, single geometry, the ground-state parameterized dispersion energy is identical for both the initial and final states, resulting in exact cancellation. Consequently, the vertical energies discussed herein represent the intrinsic performance of the pure B3LYP functional framework. The minor differences observed between the B3LYP//B3LYP-D3 and B3LYP//B3LYP-D3(BJ) protocols originate exclusively from the structural variations inherited from the preceding ground- or excited-state geometry optimizations. In contrast to the clearer trends observed for ground-state orbital energies—where B3LYP-D3 and B3LYP-D3(BJ) generally perform well—the performance for excited-state properties is somewhat more nuanced. In this context, tuning the range-separation parameter in ωB97XD can, in some cases, improve predictive capability; however, the overall improvement is typically modest and should be weighed against the additional computational effort required by the tuning procedure. The following discussion provides a detailed assessment of these trends.

Following ground-state optimizations, the singlet-state emission energies (S_1^{em}) were evaluated for all investigated compounds. In this work, fluorescence energies were obtained from optimized S_1 geometries followed by vertical emission calculations. Thus, excited-state structural relaxation was included. Although these values do not correspond directly to experimental λ_{max}, which are influenced by vibronic structure, finite-temperature effects, and environmental broadening. A rigorous comparison with experimental band maxima would require vibronic simulations and spectral-shape modeling. Therefore, computed transition energies should not be interpreted as simulated λ_{max} values. For triplet energies, we primarily relied on vertical excitation energies (and emission estimates where applicable), without systematically performing full T_1 geometry optimizations for the entire dataset. The adiabatic triplet energies and vibronic effects would provide a more direct comparison to phosphorescence maxima. However, including full excited-state optimizations and spectral simulations for all 26 molecules and multiple functionals would substantially extend the scope of the present benchmarking study. We employed linear-response PCM (LR-PCM) consistently across all methods to maintain a controlled comparison. We recognize that, for charge-transfer states—particularly in

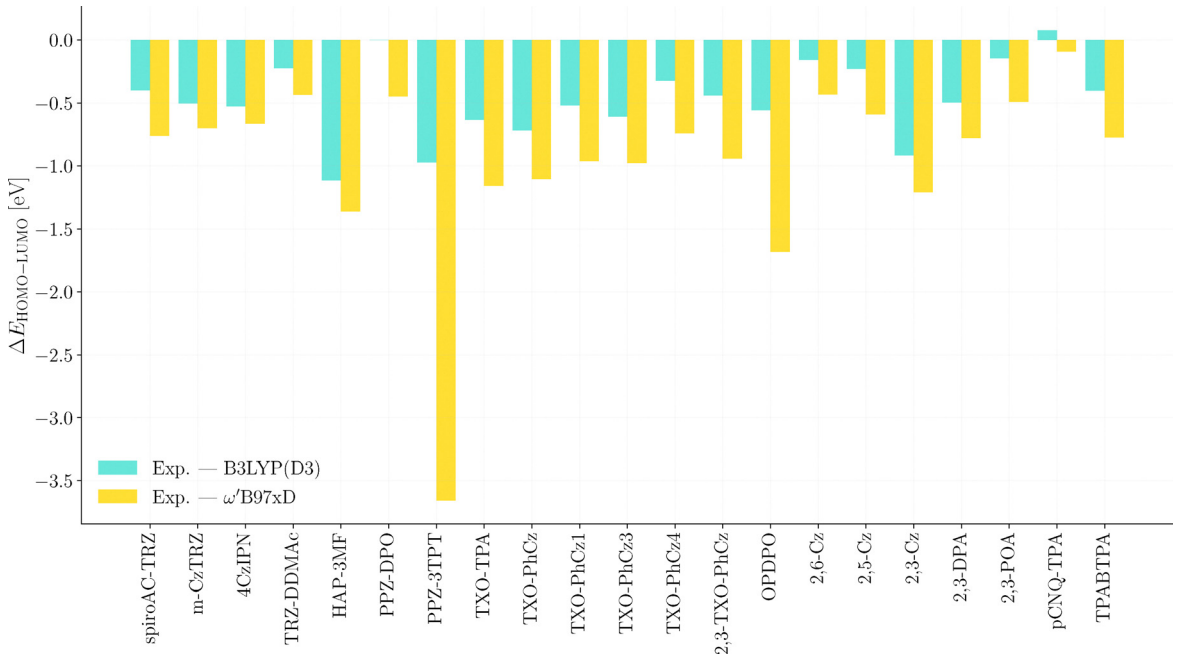

Fig. 2 Comparison of deviations between experimental and computed HOMO–LUMO gaps ($\Delta E_{\mathrm{HOMO-LUMO}}$) obtained using the B3LYP-D3 (blue) and ω′B97XD (yellow) functionals.

emission—standard LR-PCM can be inadequate due to the lack of state-specific polarization.

Analysis of the RMSD values (Table 1) indicates that tuned-ω′B97XD performs somewhat better (RMSD = 0.45 eV) than B3LYP-D3 (RMSD $\approx$ 0.64 eV), with a marginal reduction in standard deviation (difference of $\sim$0.05 eV). M06-2X yields even smaller MAD values than both B3LYP-D3 and B3LYP-D3(BJ), whereas the default-ωB97XD functional again performs the poorest (MAD = 0.68 eV). Molecule-wise deviations between B3LYP-D3 and tuned ω′B97XD (Fig. S6) further reinforce these trends: for most compounds, tuned-ω′B97XD (yellow bars) provides smaller deviations than B3LYP-D3 (blue bars). Pronounced deviations are, however, observed for specific cases—TXO-PHCz1 (deviation = 1.17 eV) and HAP-3MF (−0.91 eV)—under the tuned functional. Fig. S7 shows that M06-2X generally outperforms both B3LYP-D3(BJ) and default ωB97XD, except for spiroAC-TRZ and OPDPO. These results underscore the importance of long-range corrections, such as those incorporated in M06-2X and tuned-ω′B97XD, for improved modeling of excited-state emission energies.

For singlet-state absorption energies, tuned-ω′B97XD provides the most accurate description (MAD = 0.34 eV; RMSE = 0.42 eV), closely followed by B3LYP-D3(BJ) (Table 1). Here, M06-2X performs slightly worse than the B3LYP-based functionals, while the default-ωB97XD again shows the most significant discrepancies. Fig. S8 and S9 further visualize these trends. In particular, although B3LYP-D3 generally surpasses M06-2X in terms of MAD and RMSE, M06-2X delivers better performance for selected molecules such as spiroAC-TRZ, 3DPA3ACN, TXO-PhCz1, TXO-PhCz4, 2,3-TXO-PhCz, 2,6-Cz, and 2,3-POA. The complete sets of gas-phase S_1 absorption and emission energies are provided in Tables S5 and S6.

Inclusion of solvent effects for a representative subset (Tables S7 and S8) yields mixed outcomes: solvation improves MAD values for B3LYP-D3(BJ), M06-2X, and tuned ω′B97XD in the case of emission energies but deteriorates the accuracy of the remaining functionals; for absorption energies, solvation improves M06-2X and default ωB97XD but slightly worsens the performance of the other three methods. These observations highlight limited but observable solvent-induced corrections, which are not the primary focus of this work. Overall, the vertical photophysical properties obtained *via* the B3LYP//B3LYP-D3 and B3LYP//B3LYP-D3(BJ) protocols are nearly identical across the investigated dataset. This high degree of similarity indicates that the choice of damping function (zero-damping *vs.* Becke–Johnson damping) introduces negligible structural deviations in the optimized ground- and excited-state geometries of these TADF emitters. Because the direct dispersion energy terms cancel out entirely within the vertical approximation, these closely matching transition energies are a direct reflection of the highly similar underlying molecular conformations.

We now turn to the singlet–triplet energy gap ΔE_{ST}, which is arguably the most critical descriptor among the excited-state properties considered, as values near or below 0.2 eV are essential for enabling thermally activated delayed fluorescence.[11,18] Following common practice, ΔE_{ST} was computed from single-point energy differences between the optimized S_1 and T_1 states—a computationally efficient and widely validated approach.[8,9,19,20] As shown in Table 1, B3LYP-D3 and B3LYP-D3(BJ) again yield the smallest deviations (MAD = 0.10–0.11 eV; RMSD = 0.13 eV). By contrast, the default ωB97XD functional performs notably worse (MAD = 0.66 eV; RMSD = 0.67 eV). Although tuning ω′B97XD substantially reduces the error, the tuned variant still does not

Fig. 3 Comparison of molecule-wise deviations between experimental and computed singlet–triplet energy gaps (ΔE_{ST}) using B3LYP-D3 (blue) and tuned ω′B97X-D (yellow). Positive deviations indicate overestimation. The results highlight the robust performance of B3LYP-D3 and the partially improved, though not uniformly superior, accuracy achieved through ω-tuning.

surpass the B3LYP-based approaches. Fig. 3 provides molecule-wise comparisons: deviations obtained from tuned ω′B97XD (yellow) remain larger than those from B3LYP-D3 (blue) for most molecules, except 3DPA3ACN and 4CzIPN. Significant deviations (>0.2 eV) are observed for OPDPO with both functionals, likely due to the presence of a phosphorus atom—the only such motif in this dataset. PPZ-3TPT displays contrasting deviations for the two methods, with one overestimating and the other underestimating the experimental value. Most B3LYP-D3 predictions lie within 0.1 eV, except for compounds such as 3DPA3ACN, PPZ-3TPT, OPDPO, 2,3-DPA, and pCNQ-TPA. Additional comparisons (Fig. S10) confirm that B3LYP-D3(BJ) outperforms M06-2X and ωB97XD, both of which show larger deviations. The corresponding values of ΔE_{ST} are provided in Table S9 in the SI.

Taken together, the excited-state results reveal a more balanced picture than that derived from ground-state properties: tuning the range-separation parameter in ω′B97XD generally improves performance for absorption and emission energies and yields accuracy comparable to B3LYP-D3 for ΔE_{ST}. Nevertheless, the improvements relative to B3LYP-based functionals are typically modest, not universal across properties or molecules, and should be weighed against the additional computational effort required to tune. When evaluated across both ground- and excited-state properties, B3LYP-D3 and B3LYP-D3(BJ) provide consistently reliable results with comparatively low computational cost, making them practical choices for predicting the range of properties examined in this study. When utilizing these dispersion corrections for excited-state geometry optimizations (*e.g.*, within the TD-DFT framework), a crucial theoretical caveat must be highlighted. Standard formulations such as D3, D3(BJ), and D2 are fundamentally ground-state corrections. Because they are driven purely by nuclear coordinates and ground-state atomic parameters, they do not account for the changes in dynamic polarizabilities that accompany electronic excitation. As documented by Grimme and Hühnerbein, as well as in recent comprehensive benchmarks on excimers and exciplexes by Goerigk and co-workers, these terms offer only a crude approximation of dispersion effects within excited-state potential energy surfaces.[61–65] Nevertheless, their inclusion during excited-state structural relaxation remains a common and practical protocol in contemporary photophysical simulations, serving as a vital baseline that is generally preferable to neglecting non-covalent London dispersion forces entirely.

3.3 Radiative and non-radiative rate constants

Following the evaluation of excited-state energies, we next examined the photophysical rate constants governing fluorescence and TADF processes. Because the computation of radiative and non-radiative rates depends on several key descriptors---including oscillator strengths, spin–orbit coupling elements, singlet–triplet energy gaps, and reorganization energies within the Marcus framework—we focused on B3LYP-D3 and tuned-ω′B97XD. These two functionals demonstrated the closest performance in earlier benchmarks and thus provide a meaningful basis for assessing whether the computationally demanding tuning step yields significant practical improvements for rate predictions.

Fluorescence, intersystem crossing, and reverse intersystem crossing rate constants were computed using the expressions detailed in the Method section. The resulting rates are listed in Table S10, and ISC/RISC rates are reported in Table S11. Fig. 4 compares the calculated and experimental fluorescence rates.

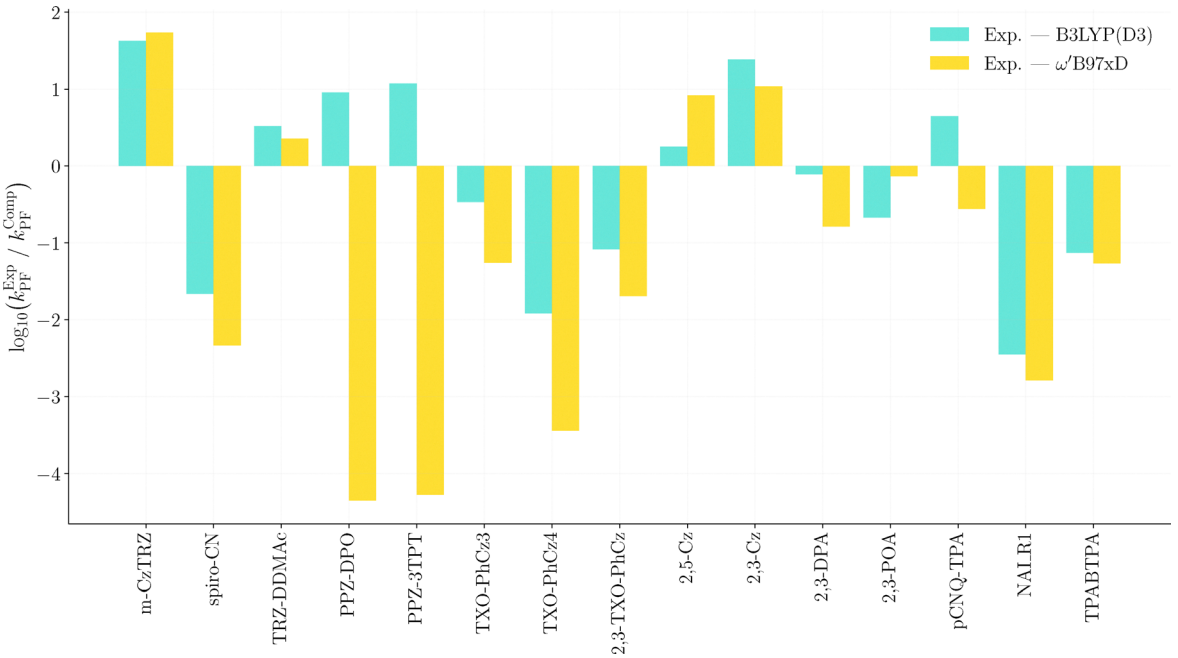

Fig. 4 Comparison of deviations between experimental k_{PF} values and those computed using the B3LYP-D3 functional (blue) and tuned-ω'B97XD functional (yellow).

The vertical axis shows $\log(k_{exp}/k_{comp})$, where a value of zero represents perfect agreement. Positive deviations indicate an underestimation of the rate by theory, whereas negative deviations denote overestimation. Both under- and overestimation trends are observed across the dataset; however, B3LYP-D3 (blue symbols) consistently exhibits smaller deviations than tuned-ω'B97XD (yellow symbols), with only two notable exceptions (TRZ-DDMAc and pCNQ-TPA). Although tuned-ω'B97XD improves accuracy marginally in certain isolated cases, these improvements are not systematic and do not outweigh the substantial additional cost of performing molecule-specific ω-tuning.

A similar comparison was carried out for nonradiative processes. Fig. S11 and S12 show the ISC and RISC rate constants computed with both functionals. Due to the limited experimental data available for these quantities, the comparison focuses solely on theoretical predictions. The logarithmic plots show that B3LYP-D3 and tuned-ω'B97XD generally produce ISC and RISC rates of the same order of magnitude. For many molecules, the data points from the two functionals overlap nearly exactly, reflecting their comparable performance in describing spin-forbidden transitions. Although variations appear for a few specific systems, the overall consistency across the dataset confirms that B3LYP-D3 captures the essential trends in both radiative and nonradiative dynamics.

Taken together, these results suggest that while ω-tuning can improve excited-state properties in certain cases, its advantage does not necessarily translate into a consistent improvement in rate predictions. Considering the additional computational effort associated with tuning and the relatively modest accuracy gains observed, B3LYP-D3 provides a reliable and computationally efficient option for estimating photophysical rate constants in TADF systems.

4 Exciton characteristics

One of the defining features of donor–acceptor–donor systems is their characteristic long-range charge-transfer (LRCT) behaviour, which can be evaluated both qualitatively through density-difference plots and quantitatively using charge-transfer descriptors such as the charge-transfer number (Q_{CT}) and the distance between the negative and positive barycentres (D_{CT}) during the $S_1 \rightarrow S_0$ transition. In this study, both descriptors were employed to assess the degree of charge separation and exciton localization across the investigated molecules.

It is important to note that the calculated exciton charge-transfer (CT) descriptors are entirely determined by the choice of the underlying exchange–correlation functional, rather than by empirical dispersion corrections. Because standard dispersion schemes (such as Grimme's D2 or D3) are additive, geometry-dependent energy terms, they exert no influence on the Kohn–Sham orbitals or the resulting electronic wavefunction. Consequently, the variations observed in the CT descriptors across the different protocols are fundamentally driven by the treatment of electron exchange—specifically the presence of range-separation and the fraction of exact Hartree–Fock exchange within the functional—which dictates the spatial localization and overlap of the transition densities. The negligible differences observed between the B3LYP//B3LYP-D3 and B3LYP//B3LYP-D3(BJ) protocols are strictly indirect consequences of the minor structural deviations in their underlying optimized geometries.

To obtain a qualitative picture of the charge-transfer behaviour, density-difference plots were generated using both B3LYP-D3 and tuned-ω functionals, presented in Fig. S13 and S14, respectively. Two distinct types of charge-transfer processes are typically observed in such systems: long-range charge transfer and short-range charge transfer (SRCT). LRCT is characterised by spatially well-separated electron-rich and electron-deficient lobes located on distinct molecular fragments, while SRCT arises when these lobes alternate between adjacent atoms within the same moiety.

As illustrated in Fig. S13 and S14, the majority of the investigated molecules exhibit clear LRCT features, with charge migration occurring from the donor (blue regions) to the acceptor (yellow regions). However, exceptions are observed. For example, Mol-8 displays alternating lobes consistent with SRCT behaviour, aligned with its MR-TADF nature where individual atoms—not entire fragments—function as donors or acceptors. Mol-3 exhibits mixed behavior, lying between the SRCT and LRCT regimes. These qualitative patterns are consistent across both functionals, underscoring the robustness of the analysis.

For quantitative evaluation, the descriptors Q_{CT} and D_{CT} were computed. A Q_{CT} value close to 1 (typically >0.5) indicates an LRCT excitation, whereas smaller values imply a locally excited (LE) or SRCT character. Similarly, D_{CT} values greater than 1.6 Å signify LRCT behaviour, while smaller values denote LE-like excitations.[8,19,20] The results, summarized in Fig. 5, show that all investigated molecules possess Q_{CT} values above 0.7, confirming their LRCT character. Likewise, D_{CT} exceeds 1.6 Å for nearly all molecules except Mol-4, which lies below this threshold, indicating partial LE character (see Table S12).

Both functionals yield highly similarly consistent values Q_{CT} and D_{CT} values, demonstrating the reliability of the computational protocol. In general, tuned-ω produces slightly smaller Q_{CT} values compared to B3LYP-D3, reflecting marginally more localised excitons, but the overall trends remain unchanged. This close concordance highlights the reproducibility of the electronic-structure description and validates the robustness of the exciton analysis.

4.1 Overall assessment of method performance

Across the complete set of evaluated properties—ground-state energetics, excitation energies, singlet–triplet gaps, photophysical rates, and exciton descriptors—a broadly consistent pattern can be observed regarding the relative strengths of the

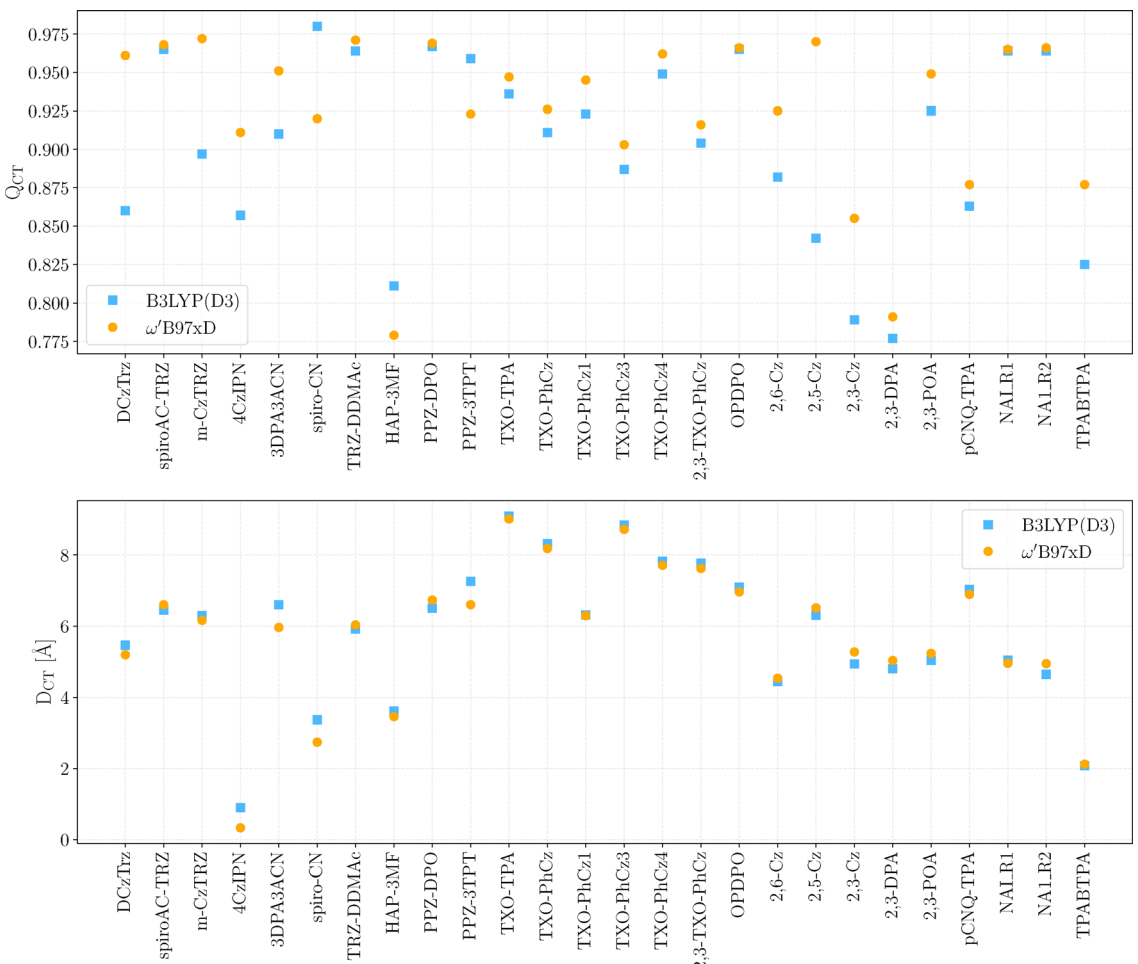

Fig. 5 Charge-transfer number (Q_{CT}) and distance between positive and negative barycentres (D_{CT}) for the investigated compounds.

tested functionals. The B3LYP-D3 family generally provides a stable and reliable reference point, offering balanced performance for both ground- and excited-state quantities with comparatively lower computational cost. Its predictions for orbital energies, ΔE_{ST}, fluorescence rates, and charge-transfer descriptors are largely consistent across the dataset, allowing it to function as a practical first-tier approach for screening and property evaluation.

Tuned long-range corrected functionals, exemplified by ω′B97X-D, can improve the description of specific excitation energies and in some cases refine charge-transfer characteristics. However, these benefits are molecule-dependent and come with increased computational overhead. In most cases, the trends produced by tuned ω and B3LYP-D3 are broadly consistent, and discrepancies seldom lead to different mechanistic interpretations of TADF behaviour. As a result, tuned ω calculations may be most useful when applied selectively—for molecules with strong long-range charge-transfer character, borderline ΔE_{ST}, or atypical electronic structure.

Photophysical rates show a similar overall pattern. B3LYP-D3 yields reasonably stable fluorescence, ISC, and RISC trends that align closely with those from tuned ω, indicating that its underlying ingredients—oscillator strengths, SOCs, and ΔE_{ST}—are captured with sufficient consistency for rate modelling. Likewise, exciton descriptors and density-difference plots exhibit very similar behavior across both methods, demonstrating that the qualitative characterization of LRCT *versus* SRCT is relatively insensitive to the choice of functional.

Taken together, these observations suggest a pragmatic two-tier strategy. B3LYP-D3 can be used as an efficient primary approach for evaluating structural, electronic, and photophysical properties across broad molecular sets. Tuned long-range corrected functionals remain useful for targeted refinement, particularly when detailed excited-state energetics or charge-transfer character must be validated. This layered approach helps balance accuracy and efficiency, ensuring that computational resources are directed where they may provide the greatest additional insight.

5 Conclusion

This study provides a comprehensive evaluation of how conventional hybrid functionals and tuned long-range-corrected functionals perform across key photophysical properties of donor–acceptor molecules. Our results show that B3LYP-based methods, particularly with dispersion corrections, deliver a consistently reliable description of ground-state electronic structure, generally outperforming the tuned-ω approach in this regime. For excited-state properties, ω-tuning offers modest improvements in some cases—most notably for absorption and emission energies—but these gains are not uniform and often yield accuracy comparable to that obtained with B3LYP-D3. Crucially, parameters central to TADF behaviour, including ΔE_{ST}, radiative and nonradiative rates, and exciton descriptors, are predicted with similar consistency by both approaches. Considering the additional computational effort and molecule-specific optimization associated with ω-tuning, the incremental improvements observed here may not always justify its routine application in large-scale computational screening. Overall, the findings indicate that B3LYP-D3 offers a practical, efficient, and broadly reliable choice for evaluating the ground- and excited-state properties of donor–acceptor systems.

In a study of this type, the observed statistical trends may reflect not only intrinsic functional performance but also the influence of methodological choices and potential error compensation. We sought to isolate, as far as practically possible, the role of the exchange—correlation functional by employing a strictly consistent computational protocol—using the same geometrical framework, basis set, solvation model, and rate formalisms across all methods. Nevertheless, we explicitly acknowledge that error compensation is inherently difficult to control and that our statistical metrics reflect a beneficial, system-specific balancing of errors. Consequently, these conclusions must be interpreted with caution, as the performance and trends identified here for these 26 TADF emitters may not be transferable to other classes of optoelectronic compounds or materials.

An expanded, more systematic benchmark that incorporates additional hybrid and range-separated hybrid formulations and analyzes their respective advantages and limitations in greater depth would further benefit the field. We therefore view the present study as a step toward such a broader assessment and anticipate pursuing a more extensive comparative investigation in future work.

Author contributions

AM conceived the problem. Sanyam, NT, and KS conducted all the simulations. Sanyam, NT, and AM analyzed the results and prepared the draft.

Conflicts of interest

There are no conflicts to declare.

Data availability

The data that support the findings of this study are available from the corresponding authors upon reasonable request.

Supplementary information (SI): additional figures and tables comparing calculated and experimental photophysical properties. Fig. S1–S5 show molecule-wise comparisons of frontier molecular orbitals, including HOMO energies (Fig. S1 and S2), LUMO energies (Fig. S3 and S4), and HOMO–LUMO gaps (Fig. S5). Emission and absorption energy comparisons are provided in Fig. S6 and S7, with solvent-corrected results shown in Fig. S8 and S9. Fig. S10 compares singlet–triplet energy gaps (ΔE_{ST}), while Fig. S11 and S12 present comparisons of ISC and RISC rates, respectively. Density difference plots obtained using the B3LYP and tuned-ω functionals are shown

in Fig. S13 and S14. Tables S1–S12 summarize the corresponding numerical data, including molecular name mappings (Table S1), HOMO, LUMO, and HOMO–LUMO gaps (Tables S2–S4), emission and absorption energies (Tables S5 and S6), solvent-corrected energies (Tables S7 and S8), ΔE_{ST} values (Table S9), experimental fluorescence rates (Table S10), ISC and RISC rates (Table S11), and excitonic characteristics (Table S12). See DOI: https://doi.org/10.1039/d6cp00979d.

Acknowledgements

The authors gratefully acknowledge the Indian Institute of Technology Gandhinagar, India, for providing research facilities and financial support. We thank PARAM Ananta for computational resources.

References

1 A. Endo, K. Sato, K. Yoshimura, T. Kai, A. Kawada, H. Miyazaki and C. Adachi, Efficient up-conversion of triplet excitons into a singlet state and its application for organic light emitting diodes, *Appl. Phys. Lett.*, 2011, **98**, 083302.
2 H. Uoyama, K. Goushi, K. Shizu, H. Nomura and C. Adachi, Highly efficient organic light-emitting diodes from delayed fluorescence, *Nature*, 2012, **492**, 234–238.
3 Y. Liu, C. Li, Z. Ren, S. Yan and M. R. Bryce, All-organic thermally activated delayed fluorescence materials for organic light-emitting diodes, *Nat. Rev. Mater.*, 2018, **3**, 1–20.
4 P. Stachelek, J. S. Ward, P. L. dos Santos, A. Danos, M. Colella, N. Haase, S. J. Raynes, A. S. Batsanov, M. R. Bryce and A. P. Monkman, Molecular Design Strategies for Color Tuning of Blue TADF Emitters, *ACS Appl. Mater. Interfaces*, 2019, **11**, 27125–27133.
5 K. Goushi, K. Yoshida, K. Sato and C. Adachi, Organic light-emitting diodes employing efficient reverse intersystem crossing for triplet-to-singlet state conversion, *Nat. Photonics*, 2012, **6**, 253–258.
6 Y. Zhang, D. Zhang, J. Wei, X. Hong, Y. Lu, D. Hu, G. Li, Z. Liu, Y. Chen and L. Duan, Achieving pure green electroluminescence with CIEy of 0.69 and EQE of 28.2% from an aza-fused multi-resonance emitter, *Angew. Chem.*, 2020, **132**, 17652–17656.
7 T. Hatakeyama, K. Shiren, K. Nakajima, S. Nomura, S. Nakatsuka, K. Kinoshita, J. Ni, Y. Ono and T. Ikuta, Ultrapure Blue Thermally Activated Delayed Fluorescence Molecules: Efficient HOMO-LUMO Separation by the Multiple Resonance Effect, *Adv. Mater.*, 2016, **28**, 2777–2781.
8 Sanyam, R. Khatua and A. Mondal, Constructing Multiresonance Thermally Activated Delayed Fluorescence Emitters for Organic LEDs: A Computational Investigation, *J. Phys. Chem. A*, 2023, **127**, 10393–10405.
9 R. Nikhitha and A. Mondal, Breaking the trade-off between ΔE_{ST} and oscillator strength in hybrid LR/SR-CT compounds for enhanced TADF performance, *J. Mater. Chem. C*, 2025, **13**, 1893–1906.
10 T. J. Penfold, E. Gindensperger, C. Daniel and C. M. Marian, Spin-vibronic mechanism for intersystem crossing, *Chem. Rev.*, 2018, **118**, 6975–7025.
11 X.-K. Chen, D. Kim and J.-L. Brédas, Thermally activated delayed fluorescence (TADF) path toward efficient electroluminescence in purely organic materials: molecular level insight, *Acc. Chem. Res.*, 2018, **51**, 2215–2224.
12 P. S. Rukin, M. Fortino, D. Prezzi and C. A. Rozzi, Complementing Adiabatic and Nonadiabatic Methods To Understand Internal Conversion Dynamics in Porphyrin Derivatives, *J. Chem. Theory Comput.*, 2024, **20**, 10759–10769.
13 D. Valverde, C. T. Ser, G. Ricci, K. Jorner, R. Pollice, A. Aspuru-Guzik and Y. Olivier, Computational Investigations of the Detailed Mechanism of Reverse Intersystem Crossing in Inverted Singlet–Triplet Gap Molecules, *ACS Appl. Mater. Interfaces*, 2024, **16**, 66991–67001.
14 J. Guan, C. Shen, J. Peng and J. Zheng, What leads to aggregation-induced emission?, *J. Phys. Chem. Lett.*, 2021, **12**, 4218–4226.
15 F. Huang, K. Wang, Y.-Z. Shi, X.-C. Fan, X. Zhang, J. Yu, C.-S. Lee and X.-H. Zhang, Approaching Efficient and Narrow RGB Electroluminescence from D–A-Type TADF Emitters Containing an Identical Multiple Resonance Backbone as the Acceptor, *ACS Appl. Mater. Interfaces*, 2021, **13**, 36089–36097.
16 H. S. Kim, S. H. Lee, S. Yoo and C. Adachi, Understanding of complex spin up-conversion processes in charge-transfer-type organic molecules, *Nat. Commun.*, 2024, **15**, 2267.
17 M. Yang, I. S. Park and T. Yasuda, Full-Color, Narrowband, and High-Efficiency Electroluminescence from Boron and Carbazole Embedded Polycyclic Heteroaromatics, *J. Am. Chem. Soc.*, 2020, **142**, 19468–19472.
18 D. Hall, S. M. Suresh, P. L. dos Santos, E. Duda, S. Bagnich, A. Pershin, P. Rajamalli, D. B. Cordes, A. M. Z. Slawin, D. Beljonne, A. Köhler, I. D. W. Samuel, Y. Olivier and E. Zysman-Colman, Improving Processability and Efficiency of Resonant TADF Emitters: A Design Strategy, *Adv. Opt. Mater.*, 2020, **8**, 1901627.
19 D. Hall, J. C. Sancho-Garca, A. Pershin, G. Ricci, D. Beljonne, E. Zysman-Colman and Y. Olivier, Modeling of multiresonant thermally activated delayed fluorescence emitters properly accounting for electron correlation is key!, *J. Chem. Theory Comput.*, 2022, **18**, 4903–4918.
20 Sanyam, R. Khatua and A. Mondal, Cost-Effective Approach for Modeling of Multiresonant Thermally Activated Delayed Fluorescence Emitters, *J. Chem. Theory Comput.*, 2023, **19**, 9290–9301.
21 O. H. Omar, X. Xie, A. Troisi and D. Padula, Identification of unknown inverted singlet–triplet cores by high-throughput virtual screening, *J. Am. Chem. Soc.*, 2023, **145**, 19790–19799.
22 K. Bhattacharyya, Can TDDFT render the electronic excited states ordering of Azine derivative? A closer investigation with DLPNO-STEOM-CCSD, *Chem. Phys. Lett.*, 2021, **779**, 138827.

23 T. Izadkhast and M. Alipour, It matters which double-hybrid is applied: On the sensitivity of singlet–triplet energy gaps in MR-TADF emitters to the ingredients of new models, *J. Chem. Phys.*, 2025, **163**, 184111.
24 R. Al-Saadon, C. Sutton and W. Yang, Accurate treatment of charge-transfer excitations and thermally activated delayed fluorescence using the particle–particle random phase approximation, *J. Chem. Theory Comput.*, 2018, **14**, 3196–3204.
25 L. Lin, Z. Wang, J. Fan and C. Wang, Theoretical insights on the electroluminescent mechanism of thermally activated delayed fluorescence emitters, *Org. Electron.*, 2017, **41**, 17–25.
26 R. Mahaan and A. John Bosco, Sulfur Oxidation State and Substituents Influenced Multifunctional Organic Luminophores in BTP Core for OLEDs: A Computational Study on RTP, TADF Emitter and Sensitizer, *J. Phys. Chem. A*, 2023, **127**, 10570–10582.
27 S. M. Pratik, V. Coropceanu and J.-L. Bredas, Enhancement of thermally activated delayed fluorescence (TADF) in multiresonant emitters *via* control of chalcogen atom embedding, *Chem. Mater.*, 2022, **34**, 8022–8030.
28 S.-H. Hwang, M. Kim, S. K. Jeon and J. Y. Lee, Stable blue thermally activated delayed fluorescent organic light-emitting diodes with three times longer lifetime than phosphorescent organic light-emitting diodes, *Adv. Mater.*, 2015, **27**, 2515–2520.
29 T.-A. Lin, T. Chatterjee, W.-L. Tsai, W.-K. Lee, M.-J. Wu, M. Jiao, K.-C. Pan, C.-L. Yi, C.-L. Chung, K.-T. Wong and C.-C. Wu, Sky-Blue Organic Light Emitting Diode with 37% External Quantum Efficiency Using Thermally Activated Delayed Fluorescence from Spiroacridine-Triazine Hybrid, *Adv. Mater.*, 2016, **28**, 6976–6983.
30 D. Liu, D. Li, H. Meng, Y. Wang and L. Wu, Multifunctional applications of triazine/carbazole hybrid thermally activated delayed fluorescence emitters in organic light emitting diodes, *J. Mater. Chem. C*, 2019, **7**, 12470–12481.
31 M. Taneda, K. Shizu, H. Tanaka and C. Adachi, High efficiency thermally activated delayed fluorescence based on 1, 3, 5-tris (4-(diphenylamino) phenyl)-2, 4, 6-tricyanobenzene, *Chem. Commun.*, 2015, **51**, 5028–5031.
32 T. Nakagawa, S.-Y. Ku, K.-T. Wong and C. Adachi, Electroluminescence based on thermally activated delayed fluorescence generated by a spirobifluorene donor–acceptor structure, *Chem. Commun.*, 2012, **48**, 9580–9582.
33 R. Braveenth, H. Lee, S. Kim, K. Raagulan, S. Kim, J. H. Kwon and K. Y. Chai, High efficiency green TADF emitters of acridine donor and triazine acceptor D–A–D structures, *J. Mater. Chem. C*, 2019, **7**, 7672–7680.
34 J. Li, Q. Zhang, H. Nomura, H. Miyazaki and C. Adachi, Thermally activated delayed fluorescence from 3nπ* to 1nπ* up-conversion and its application to organic light-emitting diodes, *Appl. Phys. Lett.*, 2014, **105**, 013301.
35 Q. Zhang, B. Li, S. Huang, H. Nomura, H. Tanaka and C. Adachi, Efficient blue organic light-emitting diodes employing thermally activated delayed fluorescence, *Nat. Photonics*, 2014, **8**, 326–332.
36 H. Wang, L. Xie, Q. Peng, L. Meng, Y. Wang, Y. Yi and P. Wang, Novel thermally activated delayed fluorescence materials–thioxanthone derivatives and their applications for highly efficient OLEDs, *Adv. Mater.*, 2014, **26**, 5198–5204.
37 X. Wei, Y. Chen, R. Duan, J. Liu, R. Wang, Y. Liu, Z. Li, Y. Yi, Y. Yamada-Takamura and P. Wang, *et al.*, Triplet decay-induced negative temperature dependence of the transient photoluminescence decay of thermally activated delayed fluorescence emitter, *J. Mater. Chem. C*, 2017, **5**, 12077–12084.
38 X. Wei, Z. Li, T. Hu, R. Duan, J. Liu, R. Wang, Y. Liu, X. Hu, Y. Yi, P. Wang and Y. Wang, Substitution conformation balances the oscillator strength and singlet–triplet energy gap for highly efficient D–A–D thermally activated delayed fluorescence emitters, *Adv. Opt. Mater.*, 2019, **7**, 1801767.
39 X. Chen, Z. Yang, Z. Xie, J. Zhao, Z. Yang, Y. Zhang, M. P. Aldred and Z. Chi, An efficient yellow thermally activated delayed fluorescence emitter with universal applications in both doped and non-doped organic light-emitting diodes, *Mater. Chem. Front.*, 2018, **2**, 1017–1023.
40 X.-F. Luo, F.-L. Li, J.-W. Zou, Q. Zou, J. Su, M.-X. Mao and Y.-X. Zheng, A series of fused carbazole/carbonyl based blue to yellow-green thermally activated delayed fluorescence materials for efficient organic light-emitting diodes, *Adv. Opt. Mater.*, 2021, **9**, 2100784.
41 Z. Li, D. Yang, C. Han, B. Zhao, H. Wang, Y. Man, P. Ma, P. Chang, D. Ma and H. Xu, Optimizing Charge Transfer and Out-Coupling of A Quasi-Planar Deep-Red TADF Emitter: towards Rec. 2020 Gamut and External Quantum Efficiency beyond 30%, *Angew. Chem. Int. Ed.*, 2021, **60**, 14846–14851.
42 W. Zeng, T. Zhou, W. Ning, C. Zhong, J. He, S. Gong, G. Xie and C. Yang, Realizing 22.5% external quantum efficiency for solution-processed thermally activated delayed-fluorescence OLEDs with red emission at 622 nm *via* a synergistic strategy of molecular engineering and host selection, *Adv. Mater.*, 2019, **31**, 1901404.
43 X. Chen, Z. Yang, W. Li, Z. Mao, J. Zhao, Y. Zhang, Y.-C. Wu, S. Jiao, Y. Liu and Z. Chi, Nondoped red fluorophores with hybridized local and charge-transfer state for high-performance fluorescent white organic light-emitting diodes, *ACS Appl. Mater. Interfaces*, 2019, **11**, 39026–39034.
44 H. Sun, C. Zhong and J.-L. Bredas, Reliable prediction with tuned range-separated functionals of the singlet–triplet gap in organic emitters for thermally activated delayed fluorescence, *J. Chem. Theory Comput.*, 2015, **11**, 3851–3858.
45 T. J. Penfold, On predicting the excited-state properties of thermally activated delayed fluorescence emitters, *J. Phys. Chem. C*, 2015, **119**, 13535–13544.
46 M. Alipour and T. Izadkhast, Toward highly efficient hyperfluorescence-based emitters through excited-states alignment using novel optimally tuned range-separated models, *Phys. Chem. Chem. Phys.*, 2022, **24**, 23718–23736.

47 M. J. Frisch, G. W. Trucks, H. B. Schlegel, G. E. Scuseria, M. A. Robb, J. R. Cheeseman, G. Scalmani, V. Barone, B. Mennucci, G. A. Petersson, H. Nakatsuji, M. Caricato, X. Li, H. P. Hratchian, A. F. Izmaylov, J. Bloino, G. Zheng, J. L. Sonnenberg, M. Hada, M. Ehara, K. Toyota, R. Fukuda, J. Hasegawa, M. Ishida, T. Nakajima, Y. Honda, O. Kitao, H. Nakai, T. Vreven, J. A. Montgomery., J. E. Peralta, F. Ogliaro, M. Bearpark, J. J. Heyd, E. Brothers, K. N. Kudin, V. N. Staroverov, R. Kobayashi, J. Normand, K. Raghavachari, A. Rendell, J. C. Burant, S. S. Iyengar, J. Tomasi, M. Cossi, N. Rega, J. M. Millam, M. Klene, J. E. Knox, J. B. Cross, V. Bakken, C. Adamo, J. Jaramillo, R. Gomperts, R. E. Stratmann, O. Yazyev, A. J. Austin, R. Cammi, C. Pomelli, J. W. Ochterski, R. L. Martin, K. Morokuma, V. G. Zakrzewski, G. A. Voth, P. Salvador, J. J. Dannenberg, S. Dapprich, A. D. Daniels, Farkas, J. B. Foresman, J. V. Ortiz, J. Cioslowski and D. J. Fox, *Gaussian 09 Revision E.01*, Gaussian Inc., Wallingford CT, 2009.

48 J.-D. Chai and M. Head-Gordon, Long-range corrected hybrid density functionals with damped atom–atom dispersion corrections, *Phys. Chem. Chem. Phys.*, 2008, **10**, 6615–6620.

49 M. Walker, A. J. Harvey, A. Sen and C. E. Dessent, Performance of M06, M06-2X, and M06-HF density functionals for conformationally flexible anionic clusters: M06 functionals perform better than B3LYP for a model system with dispersion and ionic hydrogen-bonding interactions, *J. Phys. Chem. A*, 2013, **117**, 12590–12600.

50 S. Grimme, A. Hansen, J. G. Brandenburg and C. Bannwarth, Dispersion-corrected mean-field electronic structure methods, *Chem. Rev.*, 2016, **116**, 5105–5154.

51 J. Tirado-Rives and W. L. Jorgensen, Performance of B3LYP density functional methods for a large set of organic molecules, *J. Chem. Theory Comput.*, 2008, **4**, 297–306.

52 O. A. Vydrov and G. E. Scuseria, Assessment of a long-range corrected hybrid functional, *J. Chem. Phys.*, 2006, **125**, 234109.

53 T. M. Henderson, A. F. Izmaylov, G. Scalmani and G. E. Scuseria, Can short-range hybrids describe long-range-dependent properties?, *J. Chem. Phys.*, 2009, **131**, 044108.

54 L. Kronik, T. Stein, S. Refaely-Abramson and R. Baer, Excitation gaps of finite-sized systems from optimally tuned range-separated hybrid functionals, *J. Chem. Theory Comput.*, 2012, **8**, 1515–1531.

55 Z. Zheng, D. A. Egger, J.-L. Bredas, L. Kronik and V. Coropceanu, Effect of solid-state polarization on charge-transfer excitations and transport levels at organic interfaces from a screened range-separated hybrid functional, *J. Phys. Chem. Lett.*, 2017, **8**, 3277–3283.

56 L. Kronik, Z. Zheng, D. Egger, J.-L. Bredas and V. Coropceanu, Solid-State Polarization, Charge-Transfer Excitations and Transport Levels at Organic Interfaces from a Screened Range-Separated Hybrid Functional. APS March Meeting Abstracts, 2018, pp. C56–002.

57 D. Hall, J. C. Sancho-Garca, A. Pershin, D. Beljonne, E. Zysman-Colman and Y. Olivier, Benchmarking DFT functionals for excited-state calculations of donor–acceptor TADF emitters: insights on the key parameters determining reverse inter-system crossing, *J. Phys. Chem. A*, 2023, **127**, 4743–4757.

58 Sanyam and A. Mondal, Decoding vibrational contributions and exciton dynamics in TADF emitters for enhanced OLED efficiency, *ACS Appl. Electron. Mater.*, 2025, **7**, 4843–4854.

59 T. Lu and F. Chen, Multiwfn: A multifunctional wavefunction analyzer, *J. Comput. Chem.*, 2012, **33**, 580–592.

60 A. Gonis, On the validity of Janak's theorem and ground state energies of ensembles of interacting quantum N-particle systems, *World J. Condens. Matter Phys.*, 2014, **4**, 78–83.

61 S. Sebastian, V. Riley, B. Wanniarachchi, C. Ritchie and L. Goerigk, Spin-scaled double hybrids with long-range correction solve the TD-DFT overestimation problem in BODIPY dyes: benchmarking and experimental validation, *RSC Adv.*, 2025, **15**, 22419–22431.

62 A. C. Jones and L. Goerigk, Exploring non-covalent interactions in excited states: beyond aromatic excimer models, *Phys. Chem. Chem. Phys.*, 2024, **26**, 25192–25207.

63 L. Goerigk, *Benchmarking modern density functionals for broad applications in chemistry*, Elsevier, 2024.

64 R. Huenerbein and S. Grimme, Time-dependent density functional study of excimers and exciplexes of organic molecules, *Chem. Phys.*, 2008, **343**, 362–371.

65 A. C. Jones, T. F. Loeff, B. J. Heath and L. Goerigk, Rare-gas excimers and exciplexes: Surprising challenges for time-dependent Density Functional Theory approaches, *Polyhedron*, 2025, **280**, 117678.

